13th CIRP Conference on Photonic Technologies [LANE 2024], 15-19 September 2024, Fürth, Germany

Solidification of quaternary X5CrNi18-10 alloy after laser beam welding: A phase-field approach

Muhammad Umar[a,b,*], Daniel Schneider[a,c], Britta Nestler[a,b,c]

[a]Institute for Digital Materials Science (IDM), Karlsruhe University of Applied Sciences, Moltkestraße 30, 76133 Karlsruhe, Germany
[b]Institute for Applied Materials - Microstructure Modelling and Simulation (IAM-MMS), Karlsruhe Institute of Technology (KIT), Straße am Forum 7, 76131 Karlsruhe, Germany
[c]Institute of Nanotechnology – Microstructure Simulations (INT), Karlsruhe Institute of Technology (KIT), Hermann-von-Helmholtz-Platz 1, 76344 Eggenstein-Leopoldshafen, Germany

* Corresponding author. Tel.: +49-721-925-1534. E-mail address: Muhammad.umar@h-ka.de

Abstract

The austenitic stainless steel (X5CrNi18-10) is the most commonly used chrome-nickel steel, due to its high corrosion resistance. However, it faces the challenge of cracking events during post-laser-beam-welding dendritic solidification. These microstructural changes significantly impact the final mechanical properties. To contribute to a more precise understanding of the physical mechanisms of the appearance of cracking, the goal of this research is to investigate various aspects at the microscale influenced by process-specific extreme thermal conditions. A thermodynamic model of quaternary alloy configuration is used to study the micro-segregation behavior of alloying elements and resulting morphology based on the local thermal conditions. For this purpose, a multi-component and multiphase-field-based grand chemical potential model is used. It is observed that in addition to global processing conditions, local conditions are also important to consider and classify the morphology changes from columnar-dendritic to cellular along the liquidus isotherm of the weld pool.

1. Introduction

Laser beam welding is a widely adopted joining technique in various industries due to its advantages such as high energy efficiency, low heat input, and precise control over the welding process. However, the rapid heating and cooling cycles associated with laser beam welding can lead to complex microstructural changes and solidification behavior in the weld metal, which can significantly impact the mechanical properties of the joint [1].

The X5CrNi18-10 stainless steel is a commonly used material in various applications, including the automotive, aerospace, and chemical industries, owing to its excellent corrosion resistance and mechanical properties [2]. Understanding the solidification behavior of this alloy after

laser welding is crucial for optimizing the welding process and ensuring the integrity of the welded structures.

In this study, we investigate the solidification behavior of a quaternary X5CrNi18-10 alloy after laser beam welding by means of a phase-field approach. The phase-field method is a powerful computational tool, frequently adopted over past two decades, that accurately simulates the complex microstructural patterns during phase transformation, considering the effects of alloying elements and thermal history [3]. The high concentration and thermal gradients ahead of the moving solid-liquid interface cause instabilities which sometimes accumulate to form tree like structures called dendrites. Solidification cracking is one of the consequences of such a complex dendritic morphology evolving under extreme thermal conditions as existing during welding [4].

The first mathematical model to describe the dendritic microstructure was presented in 1947 by Ivantsov which is still used for the validation of theoretical and simulation results of thermal dendrites [5]. Due to solidification temperatures more than 1700K it is difficult to observe in-situ growth of dendritic morphology; therefore, multiple attempts have been carried out to mathematically describe the growth patterns and to numerically simulate the process [6]. With the advent of enhanced computational power and simultaneous multi-core-processing during numerical simulations the phase field method has shown practicality to accurately capture the dendrite growth patterns[7]. Although the attempts have been made to include multi-component and multi-phase configurations in phase-field simulations [8], yet there is a need to strive for computationally cost-effective ways for more accurate results within comparatively less time. Therefore, grand-potential formulation with possibility of using CALPHAD database as input for accurate chemical description of multi-component alloy to simulate phase evolution in multi-phase regimes has been presented by Choudhury et al. [9].

This work serves as a basis for setting up the grand potential based phase-field model for quaternary alloy (Fe-C-Cr-Ni) which is used for studying the effect of laser beam welding parameters on dendritic morphology, micro-segregation of alloying elements and consequent effective mechanical behavior. The goal is to provide better insights into the solidification mechanisms in the mushy zone of weld seam and the resulting microstructural features. The effect of varying local thermal conditions along the liquidous on concentration fields and dendrite attributes are presented to study critical growth regions where cracking is likely to happen. The study contributes to the development of improved welding strategies and the enhancement of the mechanical performance of the welded components.

Nomenclature

N	Number of chemical components
$a(\boldsymbol{\phi}, \nabla\boldsymbol{\phi})$	Gradient energy density at interface (J/m^3).
α, β	Phase labelling indices
ϕ_α	Phase fraction of phase alpha
$\boldsymbol{\mu}$	Chemical potential vector
$\boldsymbol{J}_{at}$	Term for anti-trapping current
$\boldsymbol{c}_\alpha$	Concentration vector of phase α
$w(\boldsymbol{\phi})$	Potential energy density at interface (J/m^3).
$h_\alpha(\boldsymbol{\phi})$	Interpolation function according to the condition $\sum h_\alpha(\boldsymbol{\phi}) = 1$

2. Thermodynamics and Phase-field model

The chemical composition in mole % of X5CrNi18-10 stainless steel is shown in table 1. It has excellent corrosion resistance due to its high chromium content which makes it an excellent choice in automotive, aerospace, and chemical industries where corrosion resistance is crucial. In addition, this alloy has favorable mechanical properties, including strength and ductility due to optimum content of nickel, which makes it a good candidate where both characteristics are needed.

Considering iron and carbon being the basic component of steel a four-component based quaternary configuration (Fe-C-Cr-Ni) of the alloy is inevitable if concentration sensitivity is to be analyzed.

Table 1. Chemical composition of X5CrNi18-10 stainless steel.

Element	Ni	C	Cr	Fe
mole %	7.586	0.092	20.28	72.04
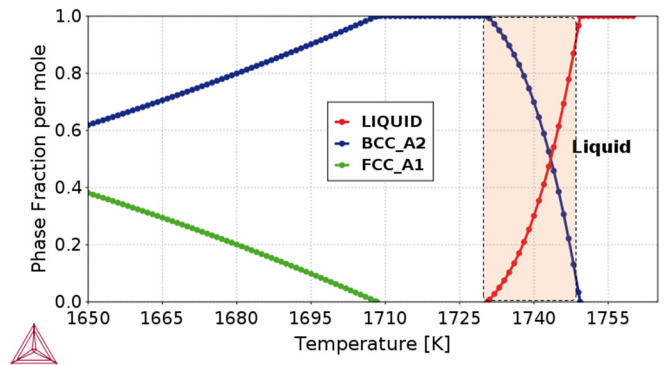
Fig. 1. Phase fraction of the alloy during solidification in mushy zone in the range 1735K and 1749K
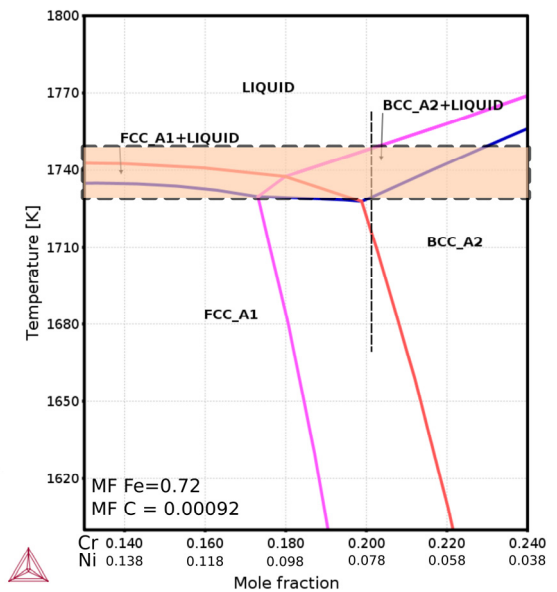
Fig. 2. Quasi-binary isopleth from quaternary (Fe-C-Cr-Ni) alloy phase diagram

For modelling of phase transformation during solidification the Gibbs energies of the phases are fitted from CALPHAD database of Liu et al. [10]. For this thermo-chemical study, a two-phase region highlighted with light orange color in the Fig. 1 and 2 is selected in the temperature range of 1735K and 1749K. The Gibbs energy functions for *liquid* and *δ-Fe* phases are fitted in second degree polynomial in this range to be used as input in the phase-field simulation study. The fitting technique is employed to get about 10x computational efficiency described in [11].

A multi-component and multi-phase field-based grand-potential formulism is applied to derive the Allen-Cahn type equations for the vector-valued Order Parameter ($\boldsymbol{\phi}$) by variations derivation reading equation (1). These phase

$$\tau\varepsilon\frac{\partial\phi_\alpha}{\partial t} = -\epsilon\left(\frac{\partial a(\boldsymbol{\phi},\nabla\boldsymbol{\phi})}{\partial\phi_\alpha} - \nabla.\frac{\partial a(\boldsymbol{\phi},\nabla\boldsymbol{\phi})}{\partial\nabla\phi_\alpha}\right) - \frac{1}{\epsilon}\frac{\partial w(\boldsymbol{\phi})}{\partial\phi_\alpha}$$
$$-\frac{\partial\psi(T,\boldsymbol{\mu},\boldsymbol{\phi})}{\partial\phi_\alpha} - \frac{1}{N}\sum_{\beta=1}^{N}-\epsilon\left(\frac{\partial a(\boldsymbol{\phi},\nabla\boldsymbol{\phi})}{\partial\phi_\beta} - \nabla.\frac{\partial a(\boldsymbol{\phi},\nabla\boldsymbol{\phi})}{\partial\nabla\phi_\beta}\right)$$
$$-\frac{1}{\epsilon}\frac{\partial w(\boldsymbol{\phi})}{\partial\phi_\beta} - \frac{\partial\psi(T,\boldsymbol{\mu},\boldsymbol{\phi})}{\partial\phi_\beta} . \quad (1)$$

evolution equations are coupled with dynamic equations of the chemical potential ($\boldsymbol{\mu}$) according to equations (2). By inverting, equation (2) related to the concentration of each component as a function of time and space.

$$\frac{\partial\boldsymbol{\mu}}{\partial t} = \left[\sum_{\alpha=1}^{N}h_\alpha(\boldsymbol{\phi})\left(\frac{\partial\boldsymbol{c}_\alpha(\boldsymbol{\mu},T)}{\partial\boldsymbol{\mu}}\right)\right]^{-1}$$
$$\cdot\begin{pmatrix}\nabla.\left(M(\boldsymbol{\phi},\boldsymbol{\mu},T)\nabla\boldsymbol{\mu} - J_{at}(\boldsymbol{\phi},\boldsymbol{\mu},T)\right) \\ -\sum_{\alpha=1}^{N}\boldsymbol{c}_\alpha(\boldsymbol{\mu},T)\frac{\partial h_a(\boldsymbol{\phi})}{\partial t} - \sum_{\alpha=1}^{N}h_\alpha(\boldsymbol{\phi})\left(\frac{\partial\boldsymbol{c}_\alpha(\boldsymbol{\mu},T)}{\partial\boldsymbol{\mu}}\right)\end{pmatrix}. \quad (2)$$

3. Results and Discussion

After theoretical validation with the classical Ivanstov's solution [12], the 2D simulation results are presented to show the morphological evolution of early solidification structure in Fig. 3. A weld geometry is shown in Fig. 3(1) having weld pool (WP), mushy zone (MZ), fusion line (FL) and partially melted zone (PMZ). Various zones (A, B, and C) shown in Fig.3 with the same labels, are considered along the liquidus line to run simulation with varying local solidification velocity. The position of the zones is precisely set from centerline (CL) to the FL in such a way that dendrite tip velocity decreases while thermal gradient increases in this sequence respectively. The dendrite tip velocity (v_d) changes according to its orientation with laser beam velocity (v_LB) according to $v\_d = v\_LB.\cos(\theta)$ [13].

The effect of local thermal conditions on dendrite morphology at different zones is shown in Fig. 3. It can be observed that merely due to orientation angle, the v_d varies from 0.0005 m/s to 0.02 m/s. Consequently, the morphology changes from plain open channel Fig. 3(B1) areas to complex inter-dendritic fused secondary dendrite arms Fig. 3(A1), respectively. With maximum v_d, the secondary dendrite arms appear and join with the counterparts from adjacent dendrites which happens to be at the CL of weld.

On the other hand, the comparatively low v_d in the regions of FL yields coarse cellular microstructure with no apparent secondary dendrite arms. This effect is enhanced as the area of observation shifts from CL towards FL. The liquid pockets trapped within the fused secondary dendrite arms may undergo delayed solidification to yield a locally different chemical segregation behaviour which is explained in Fig. 4 and 5. The dendrite growth pattern with secondary arms is picked from Fig. 3(A) for concentration distribution study as
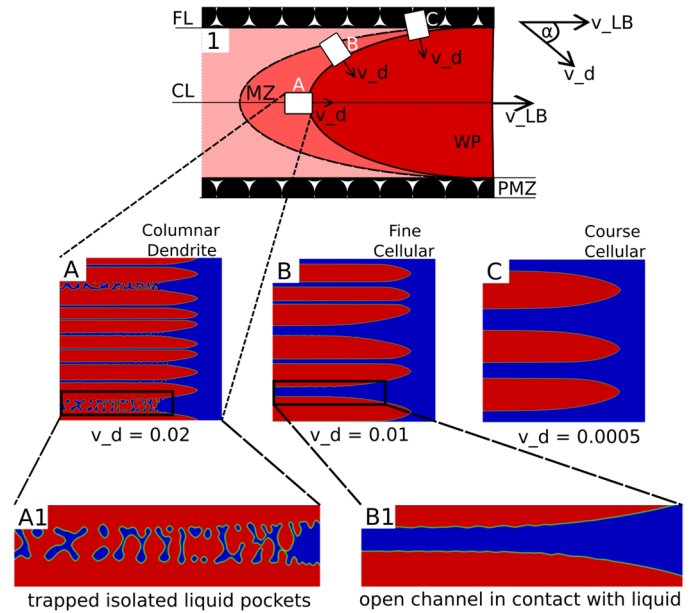
Fig. 3. Effect of local solidification velocity condition (v_d) on growth pattern of *δ-Fe* dendrite. Zones A, B and C show columnar-dendrite to cellular-dendrite transition , respectively.
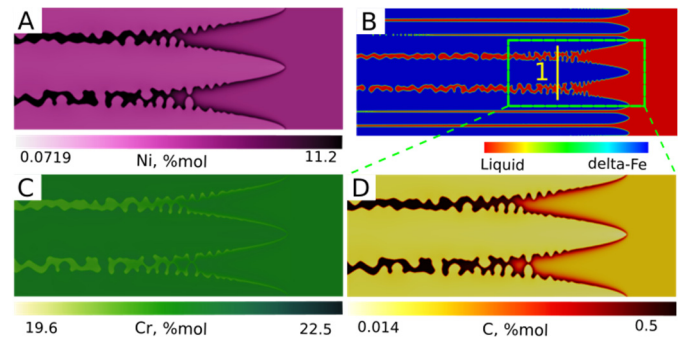
Fig. 4. Micro-segregation of alloying elements (Ni, Cr and C) in quaternary alloy at v_d =0.02 m/s in (A), (C) and (D) respectively. C and Ni are segregated in the inter-dendritic region while Cr shows deficiency there. Phase map in top right corner (B) has blue coloured *δ-Fe* dendrites while red coloured *liquid* phase in the mushy zone.
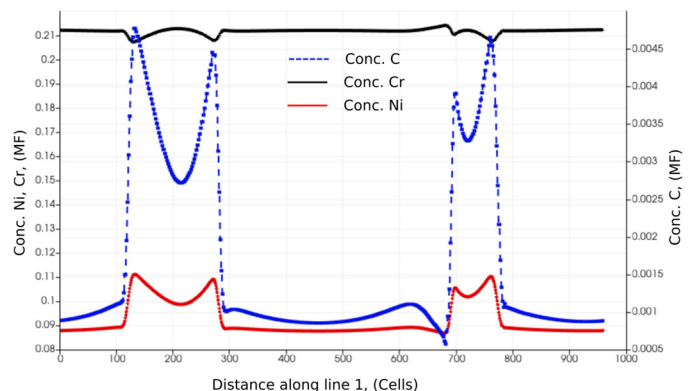
Fig. 5. Concentration line plots along line 1 in Fig. 4. Concentration of C and Cr are shown in blue and black color while for Ni red line shows the concentration gradients at all the cells along line 1.

shown in Fig. 4(B). There is liquid trapped in the inter-dendritic region within the secondary dendrite arms (Fig. 3(A1)) and accordingly the alloying elements Ni, Cr and C exhibit segregation as the dendrites grow as shown in Fig. 4. The

enlarged view of the green dotted rectangle in Fig. 4(B) is shown in the adjacent three concentration fields Fig. 4(A), (C) and (D), each for corresponding alloying element. It is clearly observable that C and Ni have higher concentration in the inter-dendritic region while a considerable deficiency is observed in the dendrite cores. Conversely, Cr shows higher concentrations within the dendrite core while inter-dendritic regions are Cr deficient.

The individual trends are more visible in the line plots in Fig. 5. The line plot for all the alloying elements show a strong jump at the interface. The chemical segregation at the interface may lead to heterogeneous mechanical properties resulting into dissociation at the interface due to eigen strains during phase transformation, in accordance with the already published results [14-16]. To computationally explore the chemo-mechanical effects and possible solidification/hot cracking events in more detail, fully coupled phase-field simulations of phase transitions, diffusion and solid mechanics are to be studied in forthcoming research work.

4. Conclusion

The investigation of local thermal conditions on dendrite morphology and micro-segregation of alloying elements in quaternary X5CrNi18-10 alloy weld pools shows that material is exposed to critical dendritic growth along the centerline. In this region secondary dendrite arms appear which trap the residual liquid and cause the strong concentration differences at the interface of the dendrites. This effect causes delayed solidification affecting the local mechanical integrity of the material during early stage of solidification, which may represent the local source points from which cracking is triggered during solidification.

Acknowledgements

References

[1]   H. Gao, G. Agarwal, M. Amirthalingam, and M. J. M. Hermans, "Hot cracking investigation during laser welding of high-strength steels with multi-scale modelling approach," *Science and Technology of Welding and Joining*, vol. 23, no. 4, pp. 287–294, May 2018, doi: 10.1080/13621718.2017.1384884.

[2]   W. Zhai, W. Zhou, Z. Zhu, and S. M. L. Nai, "Selective Laser Melting of 304L and 316L Stainless Steels A Comparative Study of Microstructures and Mechanical Properties," *Steel Res Int*, pp. 1–11, 2022.

[3]   S. Chatterjee and N. Moelans, "A grand-potential based phase-field approach for simulating growth of intermetallic phases in multicomponent alloy systems," *Acta Mater*, vol. 206, Mar. 2021, doi: 10.1016/j.actamat.2021.116630.

[4]   S. Kou, "Predicting susceptibility to solidification cracking and liquation cracking by calphad," *Metals (Basel)*, vol. 11, no. 9, Sep. 2021, doi: 10.3390/met11091442.

[5]   M. E. Glicksman, "Free Dendritic Growth," 1984.

[6]   W. Losert, B. Q. Shi, and H. Z. Cummins, "This contribution is part of the special series of Inaugural Articles by members of the Evolution of dendritic patterns during alloy solidification: Onset of the initial instability," 1998. [Online]. Available: www.pnas.org.

[7]   J. Tiaden, "Phase field simulations of the peritectic solidification of Fe-C," 1999.

[8]   B. Nestler, H. Garcke, and B. Stinner, "Multicomponent alloy solidification: Phase-field modeling and simulations," *Phys Rev E Stat Nonlin Soft Matter Phys*, vol. 71, no. 4, Apr. 2005, doi: 10.1103/PhysRevE.71.041609.

[9]   A. Choudhury and B. Nestler, "Grand-potential formulation for multicomponent phase transformations combined with thin-interface asymptotics of the double-obstacle potential," *Phys Rev E Stat Nonlin Soft Matter Phys*, vol. 85, no. 2, Feb. 2012, doi: 10.1103/PhysRevE.85.021602.

[10] W. Liu *et al.*, "Thermodynamic evaluation and investigation of solidification microstructure in the Fe–Cr–Ni–C system," *CALPHAD*, vol. 69, Jun. 2020, doi: 10.1016/j.calphad.2020.101763.

[11] K. Dargahi Noubary, M. Kellner, J. Hötzer, M. Seiz, H. J. Seifert, and B. Nestler, "Data workflow to incorporate thermodynamic energies from Calphad databases into grand-potential-based phase-field models," *J Mater Sci*, vol. 56, no. 20, pp. 11932–11952, Jul. 2021, doi: 10.1007/s10853-021-06033-7.

[12] G. P. Ivantsov, "The temperature field around a spherical, cylindrical, or pointed crystal growing in a cooling solution," vol. 58, pp. 567–569, 1947.

[13] S. Kou, "WELDING METALLURGY SECOND EDITION," 2002.

[14] F. Qayyum *et al.*, "Investigating the local deformation and transformation behavior of sintered X3CrMnNi16-7-6 TRIP steel using a calibrated crystal plasticity-based numerical simulation model," *International Journal of Materials Research*, vol. 111, no. 5, pp. 392–404, 2020, doi: 10.3139/146.111900.

[15] M. Umar, F. Qayyum, M. U. Farooq, S. Guk, and U. Prahl, "Qualitative investigation of damage initiation at meso-scale in spheroidized c45ec steels by using crystal plasticity-based numerical simulations," *Journal of Composites Science*, vol. 5, no. 8, Aug. 2021, doi: 10.3390/jcs5080222.

[16] M. Umar, F. Qayyum, M. U. Farooq, L. A. Khan, S. Guk, and U. Prahl, "Analyzing the cementite particle size and distribution in heterogeneous microstructure of C45EC steel using crystal plasticity based DAMASK code," in *Proceedings of 18th International Bhurban Conference on Applied Sciences and Technologies, IBCAST 2021*, Institute of Electrical and Electronics Engineers Inc., Jan. 2021, pp. 15–20. doi: 10.1109/IBCAST51254.2021.9393292.